Carbon 106 (2016) 306–313

Contents lists available at ScienceDirect

Carbon

journal homepage: www.elsevier.com/locate/carbon

Hierarchically nanostructured hollow carbon nanospheres for ultra-fast and long-life energy storage

Markus Klose [a, b, *], Romy Reinhold [a, b], Katja Pinkert [a], Martin Uhlemann [a], Florian Wolke [a], Juan Balach [a], Tony Jaumann [a], Ulrich Stoeck [a, b], Jürgen Eckert [a, b, 1], Lars Giebeler [a, b]

[a] Leibniz Institute for Solid State and Materials Research (IFW) Dresden e.V., Institute for Complex Materials, Helmholtzstraße 20, D-01069, Dresden, Germany
[b] Technische Universität Dresden, Institut für Werkstoffwissenschaft, Helmholtzstraße 7, D-01069, Dresden, Germany

ARTICLE INFO

Article history:
Received 13 January 2016
Received in revised form
11 May 2016
Accepted 18 May 2016
Available online 20 May 2016

ABSTRACT

We report on the successful application of porous hollow carbon nanospheres consisting of graphitic shells with a hierarchical porosity that were obtained by carbonizing an iron-containing commercially available metal-organic framework, as active material for supercapacitors. The influence of basic key parameters, such as the degree of graphitization and the accessible surface area of the carbons obtained at different temperatures, on the electrochemical performance is discussed in-depth. A high specific capacitance of 91 F g^{-1} in an aqueous electrolyte and 156 F g^{-1} using an ionic liquid is achieved. Furthermore a very steady specific capacitance over the course of 10,000 charge-discharge cycles is demonstrated. In addition, electrochemical impedance spectroscopy studies revealed that these carbons can feature a stable performance over several orders of magnitude of frequency, which render them interesting candidates for future electrochemical energy storage systems.

1. Introduction

Carbon nanostructures have been given tremendous interest by many researchers due to their possible use for a great variety of applications, such as catalysis or gas storage [1–3]. Also, a large number of different carbons and carbon structures is currently being investigated for applications in energy storage systems [4–6]. Carbon nano-onions (CNOs) represent an interesting class of materials among carbons, which exhibits a number of properties which are desirable for said application [7–10]. Firstly, due to their exohedral outer surfaces, the performance of CNOs as electrode materials is governed to a much lesser extend from limitations imposed by mass transfer kinetics, as compared to any other possible geometric arrangement of surface layers [11,12]. In addition, CNOs usually come with a high degree of graphitization, which allows for a very good electrical conductance, in turn leading to less polarization of the respective electrodes, especially at high currents [13].

However, despite these advantages, a number of challenges still remain, particularly when employing CNOs as active material in supercapacitors. Firstly, the production of CNOs is rather intricate and for the most part includes annealing nanodiamonds at very high temperatures of up to 1800 °C [14,15]. Furthermore, CNOs are mostly non-porous structures with perfectly closed graphitic layers in a concentric arrangement. Thus, the accessible surface area here can be attributed entirely to the outermost shell of the individual onions. The specific surface area of CNOs can vary between 380 and 600 m^2 g^{-1} [13,14]. This value directly correlates with the specific capacitance of the material, assuming the absence of additional contributions, such as pseudocapacitance, *via* the extend of which electrosorption can occur [16–18]. Hence, a low specific surface area of the active material somewhat limits the specific capacitance.

As shown recently, the use of a metal-organic framework (MOF) can provide access to a new spherical carbon structure with properties which are considered beneficial for energy storage applications [19,20]. Decomposing the commercially available metal-

* Corresponding author. Technische Universität Dresden, Institut für Werkstoffwissenschaft, Helmholtzstraße 7, D-01069, Dresden, Germany.
E-mail address: m.klose@ifw-dresden.de (M. Klose).
[1] Present address: Montanuniversität Leoben, Department of Material Physics, Jahnstraße 12, A-8700, Leoben, Austria and Erich Schmid Institute of Materials Science, Austrian Academy of Sciences, Jahnstraße 12, A-8700 Leoben, Austria.

http://dx.doi.org/10.1016/j.carbon.2016.05.046
0008-6223/

organic framework “Basolite F300” or “Fe-BTC” from BASF under an inert gas atmosphere yields porous carbon nanospheres (CNSs) which – in contrast to conventional CNOs – exhibit a hierarchical porosity with micropores in their shells that allow access to the inner mesoporous voids. Additionally, due to the presence of very finely dispersed iron in the precursor (MOF–) structure, catalytical graphitization takes place, leading to shell structures which feature a high degree of graphitization. It is worth noting, that this process advantageously takes place at temperatures below 1000 °C, which is a lot less than what is required for the aforementioned nanodiamond synthesis route for the production of CNOs. However, considering the overall processes of synthesizing graphitic carbon materials with a spherical morphology, the CNSs discussed in this work should be seen as an interesting new addition to the family of that kind of carbon structures which can be used in electrochemical systems, especially supercapacitors, rather than a substitute for the “classical” carbon onions.

Here, we report on the use of such MOF-derived CNSs with a hierarchical porosity as active material in electrodes for electrochemical double-layer capacitors (EDLCs). By employing these structures, considerably higher specific capacitances in an aqueous electrolyte are realized, as it is the case with conventional nonporous CNOs. It is our understanding that this work will provide the scientific community with further insight of how fine tuning the structure of carbon materials with a spherical morphology is highly advantageous for their utilization in next-generation energy storage systems.

2. Experimental section

2.1. Synthesis

For the synthesis of CNSs, Basolite F300 (CAS: 1195763-37-1) from Sigma Aldrich was used. Prior to use, the powder was further homogenized for 10 min, using a ball mill (SPEX 5100 Mixer Mill, 50 Hz). Then, 1 g of F300 was placed into an alumina combustion boat under a flow of argon, situated in a horizontal quartz glass tube furnace. A heating rate of 300 K h^{-1} was applied until the desired temperature was reached and kept for 1 h until the samples were cooled down naturally. Then, the samples were removed and kept under argon atmosphere until they were treated with 50 ml of a mixture of ethanol (Berkel AHK, 99%) and hydrochloric acid (Merck KGaA, 37%, p.A.) (1:5 v/v) for 24 h. Samples were dried and washed again using the same amount and composition of etching solution before rinsing them thoroughly with 100 ml of a water and ethanol mixture (1:5 v/v). Finally, all samples were dried at 130 °C under air for 24 h. Samples are denoted as “CNS-700”, “CNS-800” and “CNS-900”, referring to the respective temperatures at which they were synthesized.

2.2. Characterization

For X-ray powder diffraction (XRD) experiments, powder samples were glued as a thin layer on an acetate film. Data were collected in flat sample transmission mode on a STOE STADI P powder diffractometer equipped with a 6°-position sensitive detector and a curved Ge(111)-monochromator. The samples were measured with Co $K_{\alpha 1}$-radiation with a step size of $\Delta 2\theta = 0.01°$.

Transmission electron microscopy was performed, using a CM20 FEG from Philips with 200 kV acceleration voltage and a field emission gun. The powder was dispersed in ethanol and treated for 30 s in an ultrasonic bath. Afterwards the CNO dispersion was dropped onto a copper grid with a lacey carbon film with subsequent natural drying.

Nitrogen sorption experiments were carried out using a Quantachrome Quadrasorb SI. Prior to the measurement, the samples were degassed under vacuum at 423 K for 24 h. Specific surface areas were calculated at a relative pressure $p/p_0 = 0.05–0.2$ using the multi-point Brunauer–Emmett–Teller (BET) method. The total pore volume was determined at $p/p_0 = 0.97$. The pore size distributions were obtained using the Quenched Solid Density Functional Theory (QSDFT). Values for the surface area of micropores and the micropore volume were also obtained with the QSDFT method.

Raman spectra were recorded using a Thermo Scientific DXR Smart Raman spectrometer with an excitation laser wavelength of 532 nm, an effective laser power on the sample of 0.45 mW and a spot size of 2.1 μm. I_D/I_G ratios were obtained by fitting and integrating the individual peaks with Lorentzian functions *via* common data analysis software.

For element analysis of the iron-containing carbon samples, 10 mg of each carbon material was incinerated at 700 °C under air for 15 min. The residue was dissolved with hydrochloric acid and subsequently mixed with deionized water for optical emission spectroscopy (OES) analysis using an IRIS Intrepid II XUV equipped with an inductively coupled plasma (ICP) torch from Thermo Scientific.

For electrode preparation a mixture of 20 mg carbon material, 600 μl acetone (Sigma Aldrich, >99%) and 50 μl binder solution (5 wt% PVDF-21216 (Solvay) in acetone) were homogenized using an ultrasonic bath and then drop coated onto platinum current collectors (Diameter: 12 mm) before being dried for 16 h at 80 °C. Electrochemical tests were conducted at a constant temperature of 25 °C within a climate chamber, using a symmetrical two-electrode arrangement with 200 μl 1 M H_2SO_4 as electrolyte and a “Whatman”.Separator. The determination of capacitance employing an ionic liquid as electrolyte was conducted using 1-Ethyl-3-methylimidazolium tetrafluoroborate (EMIBF4) from Ionic Liquids technologies (io-li-tec) GmbH, Germany. Furthermore a multichannel VMP3 potentiostat from Bio-Logic, France was used. The capacitance was calculated using the discharge cycles of the respective experiments without employing iR compensation. For the determination of capacitance at different scan rates in CV and GCPL experiments, at each scan rate five cycles were measured, of which the last three were used for the calculation of the values presented here.

3. Results and discussion

3.1. Structural characterization

Fig. S1 (see Supporting Information SI) shows the X-ray diffraction patterns of the CNSs which were investigated for this study. While the synthesis temperatures for the samples range from 700 °C to 900 °C, there are essentially no visible crystalline features in the patterns, despite of a very small signal in the pattern of CNS-800 at approximately 30° 2θ, which might arise from crystalline graphite [21]. The absence of distinct signals from graphitic carbon in the X-ray diffraction patterns of graphitic carbon materials with a spherical morphology is well known and usually attributed to the strong curvature of the graphitic layers in the shells, as well as to the rather small size of crystalline domains [22,23].

Fig. 1 shows exemplary transmission electron micrographs of carbon CNS-800. Please note, that individual particles exhibit a distinct spherical morphology with inner voids with variable diameters of up to 80 nm. However, we acknowledge also the presence of a certain fraction of “disordered” or “amorphous” carbon being present in addition to the CNSs, as it can be seen in Fig. 1. Some residual iron from the precursor is still present, as visible for

example in the upper right corner of Fig. 1a, where the iron particle is surrounded by a carbon shell. However, results from element analysis (Table 1) indicate, that the overall amount of iron in the CNS-materials is rather minor. Furthermore in (Fig. 1b) the structure of the shells of the carbon spheres, which consists of several graphitic layers is observed. In order to quantify the amount of graphitic carbon in the CNSs, Raman spectroscopy was carried out.

Fig. 2b shows the Raman spectra of CNSs and the fitting of the contributions of several vibrational modes assigned to the individual signals. The D-Mode, located at 1340 cm^{-1}, corresponds to the presence of disordered carbon, whereas the G-Mode at 1590 cm^{-1} (for CNS-700) and 1572 cm^{-1} (for CNS-800 and CNS-900) is associated with graphitic carbon [24,25]. In addition, the D′-Mode is observed in the spectra of CNS-800 and CNS-900. The exact origin of this signal is still subject of discussion, but it is most likely designated to the curvature of the graphitic layers in the shells of the carbon spheres [26,27].

Furthermore the presence of the distinct signal arising from the D-Mode is another indication that, in addition to the highly graphitic CNS-material, disordered carbon is also present in the samples as a secondary phase. The areal ratios of the D- and G-Mode signals, the I_D/I_G-ratio, is indicative for the degree of graphitization of the respective material. In Fig. 2a, the I_D/I_G-ratios and the values for the full width at half maximum (FWHM) of D- and G-mode and their respective dependency on the synthesis temperature are displayed. With increasing order, that is with increasing size of the graphitic domains, the values for the FWHM of the vibrational modes decrease. At the same time also the I_D/I_G-ratio decreases, demonstrating an overall increase of the graphitic carbon content in those samples, which were obtained by using higher synthesis temperatures. Thus, an increasing of the synthesis temperature leads to the formation of larger graphitic domains, as well as to a larger amount thereof.

Another important feature of this type of carbon material is the porosity. In order to gain additional insights into this property nitrogen physisorption experiments were carried out. Fig. S2 shows the respective sorption isotherms together with their respective pore size distributions. All sorption isotherms indicate a quick uptake of nitrogen at low relative pressures ($p/p_0 < 0.1$) and a distinct hysteresis loop, i.e. a gap between the adsorption branch and the desorption branch. These two phenomena strongly indicate for the presence of micro- and mesopores. Moreover, the fact that the hysteresis loops close at a relative pressure of $p/p_0 = 0.42$ and their shape, which resembles “H2(a)”-Type (CNS-700), “H3”-Type (CNS-900) or a mixture of the “H3”-Type and the “H2(b)”-Type (CNS-800), is typical for the occurrence of cavitation phenomena during the desorption step [28]. In order for the cavitation effect to occur, the bottle neck-type pores in the shell have to allow an actual access to the inner voids which leads to the conclusion that those are certainly present in our material. Hence, this behavior is a result of the hierarchy of the pore system, where in this case mesopores are exclusively accessible through micropores [29,30]. Taking into account the results from electron microscopy it is clear that the shells of the onions in the CNS-materials obviously contain micropores, whereas their inner voids are mesoporous. This also means, that both the external surface area of the nanospheres, as well as the internal surface area are in fact accessible. However, at low relative pressures the entire surface area of the nanospheres (outer and inner surface area), as well as the micropores in the shells are covered with nitrogen simultaneously. Therefore no clear distinction of these different contributions to the total surface area can be made. In addition, the steady slope of the adsorption branches of the isotherms is a result of the continuous filling of (meso)pores of different sizes. This is also reflected in the rather broad pore size distributions shown in Fig. S2. However, the steep increase of uptake of nitrogen at very low relative pressures ($p/p_0 < 0.1$) cannot be explained exclusively by the microporous openings in the graphitic shells. It is our understanding that the afore mentioned disordered carbon might also exhibit a high (micro)porosity. This conclusion is further supported by the fact that the uptake of nitrogen at very low relative pressures overall decreases with increasing synthesis temperature, which is a result from the higher degree of graphitization of the carbon material which in turn leads to a smaller portion of disordered carbon being present (See also Fig. S2). It should be noted that the pronounced presence of the distinct hysteresis loops is a strong indication that the main part of the carbon material present in the samples discussed here is actually a constituent of the CNSs.

Table 1 summarizes the values regarding the porosity of the CNSs and their iron content from elemental analysis. Firstly, a general decrease of porosity with increasing synthesis temperature is evident. This finding is attributed to the higher amount of defects or micropores in the shells of the carbon spheres at lower temperature, which allow access to the inner mesopores. At higher temperatures, a higher portion of shells is closed – a process that is thermodynamically favored, consequently rendering the inner core less or even inaccessible [14,31]. This observation is consequently in-line with the results from Raman spectroscopy and XRD, as discussed above.

3.2. Electrochemical characterization

Fig. S3 shows cyclic voltammograms (CVs) of the CNSs, obtained by employing 1 M H_2SO_4 as electrolyte. At a low scan rate of 10 mV s^{-1} the CVs exhibit a nearly rectangular shape, representing the ideal behavior of electrochemical double-layer capacitors [16,32]. There are no indications of simultaneously occurring redox reactions i.e. of no pseudocapacitive contributions in any of the investigated materials. Increasing the scan rate up to 500 mV s^{-1} leads to CVs, roughly maintaining their rectangular shape, with the exception of CNS-700. It can be noted that for this sample, the resistive behavior already dominates the cell performance at a scan rate of 100 mV s^{-1}, which is especially visible at the edges of the potential window, where the reversal of the potential sweep occurs. Interestingly the resistive contributions are much lower for CNS-800 and CNS-900, where capacitive behavior is predominant.

This trend is also reflected in the specific capacitances (C_{spec}), obtained from the CV experiments (Fig. 3a). The highest capacitance, obtained from the CVs is 91 F g^{-1} for CNS-800 at a scan rate of 20 mV s^{-1}. This value drops only moderately down to 72 F g^{-1}, when the scan rate is increased 50-fold. CNS-900 starts at a lower value of 48 F g^{-1} at 10 mV s^{-1}. However, this capacitance is largely maintained, regardless of the scan rate. In contrast, CNS-700 yields initial capacitances comparable to those from CNS-800, but increasing the scan rate leads to a much more pronounced relative drop down to 33 F g^{-1} at 500 mV s^{-1}. Also, CNS-800 and CNS-900 initially yield an increase in capacitance in the CV experiments at low scan rates, which can be attributed to initial conditioning effects, such as an improved wetting of the porous carbon material during the course of the measurements [33,34]. The absolute values of the specific capacitances of the CNSs at low scan rates mainly differ due to their different specific surface areas, with CNS-900 having the lowest amount of accessible surface area. Furthermore, the relative drop of C_{spec} for the individual samples is attributed to their electrical conductivity. As illustrated in Fig. 2a, CNS-700 displays the highest value for I_D/I_G, therefore containing the lowest amount of graphitic carbon, while CNS-800 and CNS-900 show notably lower values for I_D/I_G. The difference of these materials in the ability for conducting an electrical current becomes an important influence at high scan rates, since considerably

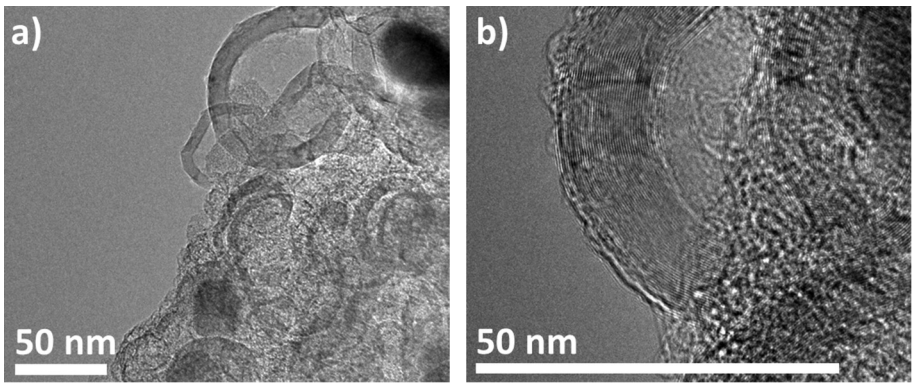

Fig. 1. Transmission electron micrographs of particles of CNS-800.

Table 1
Porosity properties and iron content for the investigated CNSs.

Sample	Surface area ($m^2\ g^{-1}$)	Surface area micropores ($m^2\ g^{-1}$)	Total pore volume ($cc\ g^{-1}$)	Micropore volume ($cc\ g^{-1}$)	Iron content (wt%)
CNS-900	491	0.01	0.87	0.05	3.95
CNS-800	770	0.03	1.05	0.18	3.02
CNS-700	943	0.05	1.05	0.18	3.03

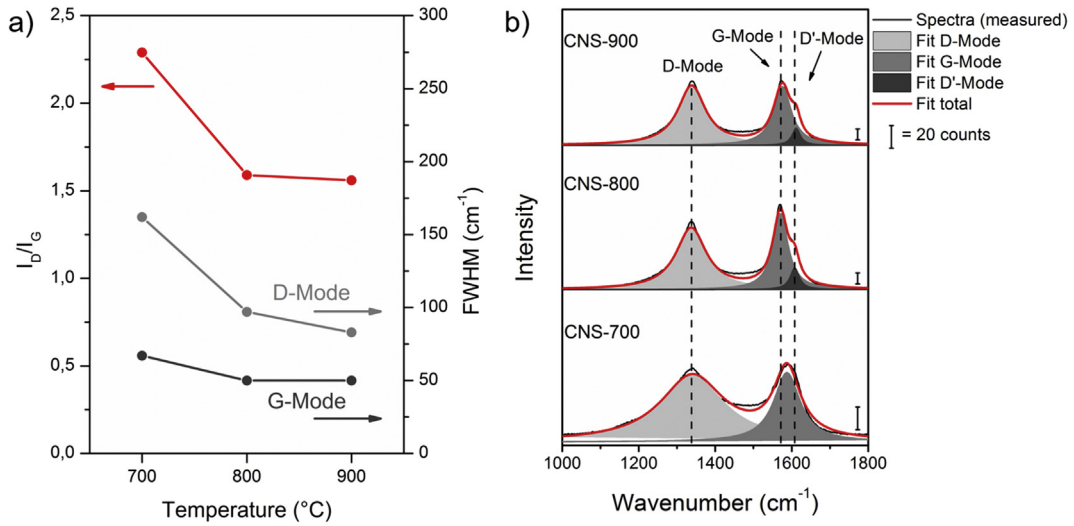

Fig. 2. a) Degree of graphitization – I_D/I_G-ratio and values for the FWHM of D- and G-mode of the CNS-samples obtained at different temperatures and **b)** Raman spectra of CNSs and fitting of the different modes. (A colour version of this figure can be viewed online.)

stronger currents emerge at this point [16,35,36].

While CV experiments help to gain important information about the basic properties of the materials, applying constant currents of different magnitudes resembles the practical conditions, under which EDLCs are used, in a more realistic way. Therefore, galvanostatic cycling with potential limitation (GCPL) was used to further characterize the CNSs. The potential window was restricted to 0.8 V due to the limited stability of the water-containing electrolyte at higher potentials. Fig. S4 contains the charge-discharge curves from GCPL measurements, whereas in Fig. 3b the corresponding specific capacitances are shown. At a low specific current of 1 A g^{-1}, all the charge-discharge curves show an overall somewhat similar behavior, with steady slopes before and after the reversal of the current at a potential of 0.8 V, which is typical for EDLCs without simultaneously occurring faradaic reactions taking place. The difference in the time that the different systems need in order to reach the upper or lower potential limit, corresponds to the extent of which electrosorption at the surfaces of the active material can occur [16,18,37]. The more pronounced the formation of that layer is, the more time will be needed for that process to be completed i.e. the longer it will take the system to reach the given potential limit. This behavior in turn corresponds to a higher specific capacitance for the respective material. At a specific current of 10 A g^{-1}, the voltage drop, which commonly occurs after reversing the current, is clearly recognized. This phenomenon is a consequence of the electrical serial resistance (ESR) of the cell, which includes, besides the capacitances, also contributions from the resistance of the active material. Since CNS-700 is expected to have the lowest electrical conductivity and hence the highest resistance, the voltage drop for this sample is much more pronounced. Consequently, the voltage drop for CNS-800 and CNS-900 appears to be less dominant but similar for both samples, since they exhibit

comparable and lower I_D/I_G-ratios as CNS-700. Therefore the progression of the specific capacitance of the CNSs under galvanostatic conditions resembles the trends that were observed in the CV experiments, both quantitatively and qualitatively (Fig. 3b).

One of the main advantages of EDLCs is their exceptional reversibility. To demonstrate the good stability of our material, long-term measurements, consisting of up to 10000 charge-discharge cycles were carried out, using CNS-800 as an example.

As shown in Fig. 4, the capacitance which is obtained from CNS-800 throughout the experiment has deteriorated by about 10% after 10000 charge-discharge events, therefore giving evidence of the promising potential of this carbon allotrope as an active material in EDLCs.

In order to gain further insight in to the working principles that govern the performance of the CNSs in supercapacitors, Electrochemical Impedance Spectroscopy (EIS) under voltage control was performed. The respective Nyquist-plot is displayed in Fig. S5. Specific capacitances were calculated, based on the principles outlined by Korenblit et al. [38] The main advantage of EIS is the determination of the response of the system, depending on the frequency of which an external stimulus, which in this case is the modulation of the potential over the equilibrium potential of the cell, is applied [16]. Fig. 5a shows the ratio of the specific capacitance of the CNS-materials and the initial capacitance C_0 at a frequency of $f = 0.002$ Hz as a function of the frequency. This allows determining the relative loss of capacitance of each carbon during the course of the experiment and thus the exclusion of effects which arise for example from different amounts of accessible specific surface area of the investigated materials. These results confirm the findings from CV- and GCPL-measurements discussed above. Again CNS-800 and CNS-900 show a very similar behavior, which is recognized in a loss of about 25% of the initial capacitance over the course of more than three orders of magnitude of frequency up to $f > 1$ Hz. After that point the capacitances drop to 25% (CNS-900) of the initial value and even lower (18%, CNS-800) at $f = 100$ Hz. In contrast, CNS-700 suffers from a pronounced loss of capacitance already at a notably lower frequency of $f = 0.1$ Hz. To our understanding, that the different behavior is strongly influenced by the different degrees of graphitization. While lower frequencies ($f < 0.1$ Hz) are dealt with reasonably well, higher frequencies lead to the appearance of stronger specific currents, which require a fast electron transport through the material in order to obtain a faster response of the system. Considering the absolute values of the capacitances obtained from the EIS measurements (Fig. 5b), the influence of the specific surface area becomes clear. Hence, CNS-800 exhibits the highest specific capacitance throughout the entire measurement, even surpassing CNS-900, regardless of the slightly lower I_D/I_G-value of CNS-800. While CNS-700 initially shows higher capacitances than CNS-900 at low frequencies, due to the higher surface area, its ability is lost to provide an adequate response once $f = 0.5$ Hz is reached.

Therefore it is reasonable to conclude that the degree of graphitization and the specific surface area both most significantly influence the performance of our CNSs in supercapacitors as the two most important parameters. However, their influence is somewhat contrary with respect to each other with increasing synthesis temperature. CNS-700 exhibits the highest specific surface area but the lowest degree of graphitization, leading to a steep loss of capacitance once higher currents are applied. In contrast, CNS-900 contains the lowest amount of specific surface area of our samples, but a much higher degree of graphitization, thus sustaining a good performance even at high currents. CNS-800 represents a very good trade-off between these two influences.

A comparison of the electrochemical performance and key parameters of the respective experiments of different graphitic carbon materials with a spherical morphology, reported previously by other groups, is presented in Table 2.

In order to ensure comparability, this table compares only materials without additional redox-active species. Also, these carbons have not been exposed to treatments that further increase the specific surface area, such as KOH- or H_2SO_4-activation. Nevertheless, CNS-800 exhibits the highest specific capacitance of these materials in aqueous electrolytes. As it was outlined before, this result is attributed to the high specific surface area, which is a result of the unique pore structure of this type of spherical carbon material, since it enables access to the inner voids of the carbon spheres. Additionally, the high degree of graphitization of our CNSs is considered as a crucial factor for the successful exploitation of the full potential of this material, becoming especially import at high currents.

While the performance of the CNSs shown here using an aqueous electrolyte is certainly remarkable, the picture is somewhat different when employing an ionic liquid as an electrolyte.

Here, as an example, CNS-800 was selected as active material together with 1-Ethyl-3-methylimidazolium tetrafluoroborate (EMIBF4) as electrolyte.

Fig. 6a shows the respective CVs at different scan rates. Already at a rather low scan rate of 10 mV s^{-1} the CV does not exhibit a rectangular shape. This behavior is even more pronounced once the scan rate is increased 10-fold. Further information on the ionic liquid EMIBF4 and its electrochemical stability window can be found in the supporting information (SI). When considering the specific capacitance derived from CV (Fig. 6b) it is noted that a capacitance of 156 F g^{-1} at a scan rate of 2 mV s^{-1} can be realized, which is the highest value for our CNSs thus far. However, with increasing the scan rate the capacitance drops to 88 F g^{-1} for 100 mV s^{-1} which is very close to the value that can be obtained using CNS-800 in the aqueous electrolyte (85 F g^{-1}, Fig. 3a).

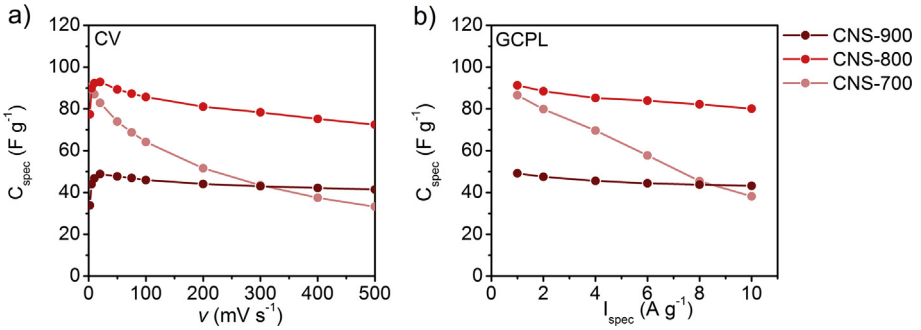

Fig. 3. Specific capacitances derived from **a)** cyclic voltammetry (CV) and **b)** galvanostatic cycling with potential limitation (GCPL) of CNSs as active material in EDLCs, using 1 M H_2SO_4 as electrolyte. (A colour version of this figure can be viewed online.)

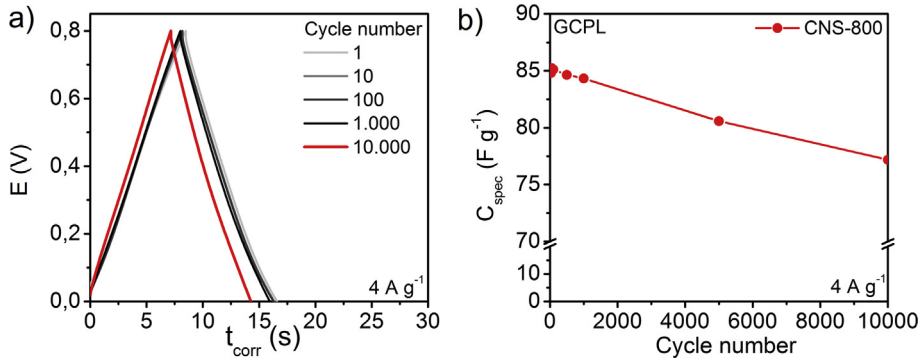

Fig. 4. a) Charge-discharge curves at different cycle numbers of CNS-800 and **b)** corresponding capacitances at a constant current of 4 A g^{-1} from long-term cycling experiments. (A colour version of this figure can be viewed online.)

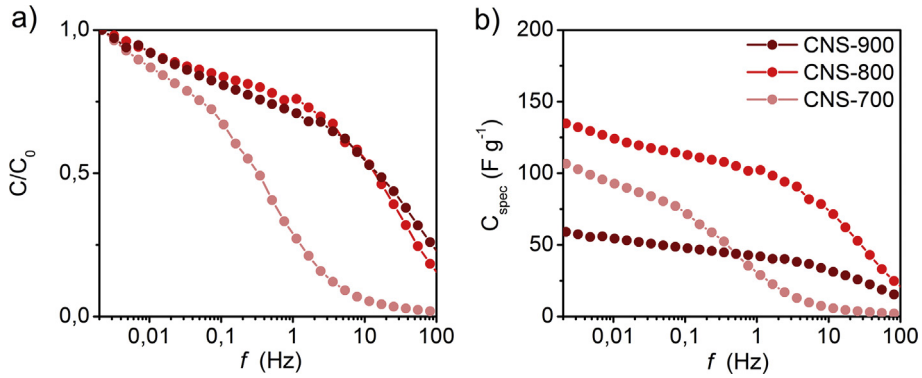

Fig. 5. a) Progression of the frequency-dependent specific capacitances in relation to the initial capacitance C_0 at $f = 0.002$ Hz and **b)** absolute values for the frequency-dependent specific capacitances of CNSs. (A colour version of this figure can be viewed online.)

Table 2
Comparison of the electrochemical performance of different graphitic carbon materials with a spherical morphology in aqueous electrolytes. Values were obtained from the respective references.

Material	Electrolyte	Test conditions	Specific surface area (m^2 g^{-1})	Capacitance (F g^{-1})	Reference
CNS-800	1 M H_2SO_4	CV, 20 mV s^{-1}	770	91	This work
Pristine CNO	2 M KNO_3	GCPL, 3 A g^{-1}	440	22	[39]
NCNO	1 M H_2SO_4	CV 20 mV s^{-1}	520	27	[40]
CNOs(1650)-AIR	0.1 M NaCl	CV, 20 mV s^{-1}	488	43	[41]
ox-CNO	0.1 M NaCl	CV, 20 mV s^{-1}	–	9	[42]
oz-CNO	0.1 M Na_2SO_4	CV, 20 mV s^{-1}	–	<43	[43]
OLC	1 M H2SO4	CV, 20 mV s^{-1}	–	20	[44]
N–CNOs	1 M H_2SO_4	CV, 20 mV s^{-1}	500	39	[45]

Interestingly, even though the use of an ionic liquid allows for a much larger potential window (3.4 V for the ionic liquid vs. 0.8 V for H_2SO_4) in which these experiments can be conducted, the overall gain in performance in marginal. The same trend is reflected in the results obtained from EIS-experiments, shown in Fig. 6c and d. The corresponding Nyquist-Plot can be found in Fig. S6. The frequency dependent capacitance can be seen steadily decreasing throughout the entire experiment, both with respect to its initial value at $f = 0.002$ Hz as well as in absolute values. It is our understanding that the higher viscosity of EMIBF4 is likely to be one of the main factors for the limited increase in performance [46]. Since in the case of the CNSs also the surface of the mesoporous inner voids of the carbon spheres contributes to the capacitance, the access to those pores can play a dominant role. However, the openings in the shells of the spheres are microporous which in turn is a limiting factor for the transport of ions especially when increasing the rate with which the device is charged and discharged and once an electrolyte with a high viscosity is used [33]. This effect could play a smaller role at higher temperatures, since the viscosity of ionic liquids is strongly temperature dependent [47]. Another important factor in this respect might be the surface functionalization of the CNSs as it governs the interaction of the active material with the ions of the electrolyte [34,48]. A detailed analysis of the surface of the CNS materials and their respective functionalization will be subject of our future work.

4. Conclusions

In conclusion, we have demonstrated the promising capabilities of MOF-derived porous CNSs as active materials in supercapacitors in aqueous electrolytes and in an ionic liquid. While very good capacitances can be obtained using an aqueous electrolyte, the

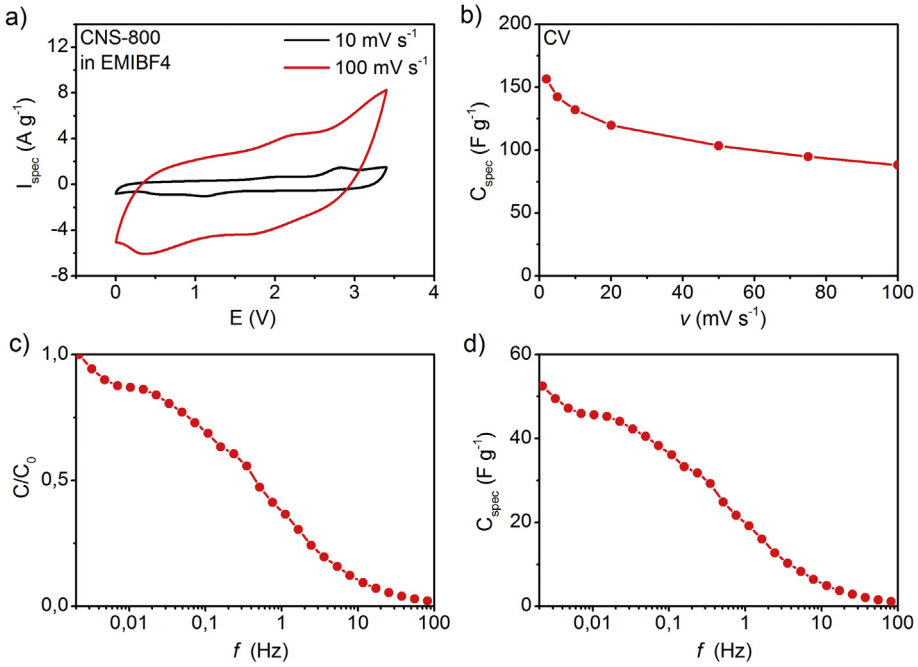

Fig. 6. a) CV-Curves at different scan rates using CNS-800 as active material and EMIBF4 as electrolyte and **b)** Specific capacitance derived from CV at different scan rates. c) Progression of the frequency-dependent specific capacitance in relation to the initial capacitance C_0 at $f = 0.002$ Hz and **d)** absolute values for the frequency-dependent specific capacitances of CNS-800. (A colour version of this figure can be viewed online.)

performance of CNS-800 in combination with an ionic liquid still holds room for improvement. Considering that the present work was focused on the basic properties of that material, it is reasonable to assume that the performance of this type of graphitic spherical carbon material can be optimized to yield even higher performances. This might be done by increasing the specific surface area by chemical activation treatments, using KOH for example [39,49,50]. Furthermore, *via* the addition of metal oxides to the CNSs, pseudocapacitive active sites can be introduced, yielding higher specific capacitances for hybrid supercapacitors [51,40]. Also, fine-tuning the synthesis conditions and procedure might allow for an increase in the overall percentage of graphitic carbon contained in the CNSs. While these modifications are beyond the scope of this report, we believe that the carbons presented here hold great potential for next-generation energy storage systems.

Acknowledgements

The authors are grateful to Andrea Voß, Anne Voidel and Ronny Buckan for elemental analysis. Further gratitude is expressed to Robert R. Rottenkügler and Mönke M. Mautzbach for valuable scientific discussion, as well as to Dr. Silke Hampel for providing the Raman spectrometer. The German Ministry of Education and Research is acknowledged for financial support within the ADNAMSES project (grant no. 01DH14002).

Appendix A. Supplementary data

Supplementary data related to this article can be found at http://dx.doi.org/10.1016/j.carbon.2016.05.046.

References

[1] R. Sharma, S.-W. Chee, A. Herzing, R. Miranda, P. Rez, Evaluation of the role of Au in improving catalytic activity of Ni nanoparticles for the formation of one-dimensional carbon nanostructures, Nano Lett. 11 (2011) 2464–2471.
[2] R. Lv, T. Cui, M.-S. Jun, Q. Zhang, A. Cao, D.S. Su, et al., Open-ended, N-Doped carbon nanotube-graphene hybrid nanostructures as high-performance catalyst support, Adv. Funct. Mater 21 (2011) 999–1006.
[3] A. Almasoudi, R. Mokaya, Preparation and hydrogen storage capacity of templated and activated carbons nanocast from commercially available zeolitic imidazolate framework, J. Mater. Chem. 22 (2012) 146–152.
[4] Y. Zhai, Y. Dou, D. Zhao, P.F. Fulvio, R.T. Mayes, S. Dai, Carbon materials for chemical capacitive energy storage, Adv. Mater 23 (2011) 4828–4850.
[5] A.J. Amali, J.-K. Sun, Q. Xu, From assembled metal–organic framework nanoparticles to hierarchically porous carbon for electrochemical energy storage, Chem. Commun 50 (2014) 1519–1522.
[6] S.L. Candelaria, Y. Shao, W. Zhou, X. Li, J. Xiao, J.-G. Zhang, et al., Nanostructured carbon for energy storage and conversion, Nano Energy 1 (2012) 195–220.
[7] W. Lian, H. Song, X. Chen, L. Li, J. Huo, M. Zhao, et al., The transformation of acetylene black into onion-like hollow carbon nanoparticles at 1000°C using an iron catalyst, Carbon 46 (2008) 525–530.
[8] C. Zhang, J. Li, E. Liu, C. He, C. Shi, X. Du, et al., Synthesis of hollow carbon nano-onions and their use for electrochemical hydrogen storage, Carbon 50 (2012) 3513–3521.
[9] K. Tang, R.J. White, X. Mu, M.-M. Titrici, P.A. van Aken, J. Maier, Hollow carbon nanospheres with a high rate capability for lithium-based batteries, Carbon 5 (2012) 400–403.
[10] M. Zeiger, N. Jäckel, V. Mochalin, V. Presser, Review: carbon onions for electrochemical energy storage, J. Mater. Chem. A 4 (2015) 3172–3196.
[11] J.K. McDonough, A.I. Frolov, V. Presser, J. Niu, C.H. Miller, T. Ubieto, et al., Influence of the structure of carbon onions on their electrochemical performance in supercapacitor electrodes, Carbon 50 (2012) 3298–3309.
[12] J. Huang, B.G. Sumpter, V. Meunier, G. Yushin, C. Portet, Y. Gogotsi, Curvature effects in carbon nanomaterials: exohedral versus endohedral supercapacitors, J. Mater. Res. 25 (2010) 1525–1531.
[13] M.E. Plonska-Brzezinska, L. Echegoyen, Carbon nano-onions for supercapacitor electrodes: recent developments and applications, J. Mater. Chem. A 1 (2013) 13703–13714.
[14] J.K. McDonough, Y. Gogotsi, Carbon onions: synthesis and electrochemical applications, Interface 22 (2013) 61–66.
[15] V.L. Kuznetsov, A.L. Chuvilin, Y.V. Butenko, I.Y. Mal'kov, V.M. Titov, Onion-like carbon from ultra-disperse diamond, Chem. Phys. Lett. 222 (1994) 343–348.
[16] F. Béguin, E. Frackowiak, Supercapacitors, Wiley-VCH, 2013.
[17] J. Zhang, X.S. Zhao, On the configuration of supercapacitors for maximizing electrochemical performance, ChemSusChem 5 (2012) 818–841.
[18] C. Prehal, D. Weingarth, E. Perre, R.T. Lechner, H. Amenitsch, O. Paris, et al., Tracking the structural arrangement of ions in carbon supercapacitor nanopores using in situ small-angle X-ray scattering, Energy Environ. Sci. 8 (2015) 1725–1735.
[19] M. Klose, K. Pinkert, M. Zier, M. Uhlemann, F. Wolke, T. Jaumann, et al., Hollow carbon nano-onions with hierarchical porosity derived from commercial metal organic framework, Carbon 79 (2014) 302–309.

[20] W. Chaikittisilp, K. Ariga, Y. Yamauchi, A new family of carbon materials: synthesis of MOF-derived nanoporous carbons and their promising applications, J. Mater. Chem. A 1 (2013) 14–19.
[21] P. Debye, P. Scherrer, Interferenzen an regellos orientierten Teilchen im Röntgenlicht, Phys. Z 17 (1916) 277–283.
[22] M. Bystrzejewski, M.H. Rummeli, T. Gemming, H. Lange, A. Huczko, Catalyst-free synthesis of onion-like carbon nanoparticles, New Carbon Mater 25 (2010) 1–8.
[23] Y. Gogotsi, V. Presser, Carbon Nanomaterials, second ed., CRC Press, 2013.
[24] S. Reich, C. Thomsen, Raman spectroscopy of graphite, Philos. Trans. Ser. A 362 (2004) 2271–2288.
[25] A.C. Ferrari, J. Robertson, Interpretation of Raman spectra of disordered and amorphous carbon, Phys. Rev. B 61 (2000) 14095–14107.
[26] A. Pimenta, M.G. Dresselhaus, M.S. Dresselhaus, L.G. Cançado, A. Jorio, R. Saito, Studying disorder in graphite-based systems by Raman spectroscopy, Phys. Chem. Chem. Phys. 9 (2007) 1276–1291.
[27] D. Roy, M. Chhowalla, H. Wang, N. Sano, I. Alexandrou, T.W. Clyne, et al., Characterisation of carbon nano-onions using Raman spectroscopy, Chem. Phys. Lett. 373 (2003) 52–56.
[28] M. Thommes, K. Kaneko, A.V. Neimark, J.P. Olivier, F. Rodriguez-Reinoso, J. Rouquerol, et al., Physisorption of gases, with special reference to the evaluation of surface area and pore size distribution (IUPAC Technical Report), Pure Appl. Chem. 87 (2015) 1051–1069.
[29] M. Thommes, Physical adsorption characterization of nanoporous materials, Chem. Ing. Tech 82 (2010) 1059–1073.
[30] C.J. Rasmussen, A. Vishnyakov, M. Thommes, B.M. Smarsly, F. Kleitz, A.V. Neimark, Cavitation in metastable liquid nitrogen confined to nanoscale pores, Langmuir 26 (2010) 10147–10157.
[31] G.C.C. Costa, J.K. McDonough, Y. Gogotsi, A. Navrotsky, Thermochemistry of onion-like carbons, Carbon 69 (2014) 490–494.
[32] A.G. Pandolfo, A.F. Hollenkamp, Carbon properties and their role in supercapacitors, J. Power Sources 157 (2006) 11–27.
[33] A. Lewandowski, A. Olejniczak, M. Galinski, I. Stepniak, Performance of carbon-carbon supercapacitors based on organic, aqueous and ionic liquid electrolytes, J. Power Sources 195 (2010) 5814–5819.
[34] K. Pinkert, M. Oschatz, L. Borchardt, M. Klose, M. Zier, W. Nickel, et al., Role of surface functional groups in ordered mesoporous carbide-derived carbon/ionic liquid electrolyte double-layer capacitor interfaces, ACS Appl. Mater. Interfaces 6 (2014) 2922–2928.
[35] O. Barbieri, M. Hahn, A. Herzog, R. Kötz, Capacitance limits of high surface area activated carbons for double layer capacitors, Carbon 43 (2005) 1303–1310.
[36] F. Beguin, V. Presser, A. Balducci, E. Frackowiak, Carbons and electrolytes for advanced supercapacitors, Adv. Mater 26 (2014) 2219–2251.
[37] J.O. Bockris, K. Müller, H. Wroblowa, Z. Kovac, Experimental and theoretical examination of methods of obtaining double-layer parameters, J. Electroanal. Chem. 10 (1965) 416–434.
[38] Y. Korenblit, M. Rose, E. Kockrick, L. Borchardt, A. Kvit, S. Kaskel, et al., High-rate electrochemical capacitors, ACS Nano 4 (2010) 1337–1344.
[39] Y. Gao, Y.S. Zhou, M. Qian, X.N. He, J. Redepenning, P. Goodman, et al., Chemical activation of carbon nano-onions for high-rate supercapacitor electrodes, Carbon 51 (2013) 52–58.
[40] R. Borgohain, J. Li, J.P. Selegue, Y.T. Cheng, Electrochemical study of functionalized carbon nano-onions for high-performance supercapacitor electrodes, J. Phys. Chem. C 116 (2012) 15068–15075.
[41] O. Mykhailiv, A. Lapinski, A. Molina-Ontoria, E. Regulska, L. Echegoyen, A.T. Dubis, et al., Influence of the synthetic conditions on the structural and electrochemical properties of carbon nano-onions, ChemPhysChem 16 (2015) 2182–2191.
[42] M.E. Plonska-Brzezinska, A. Palkar, K. Winkler, L. Echegoyen, Electrochemical properties of small carbon nano-onion films, Electrochem. Solid-State Lett. 13 (2010) K35–K38.
[43] M.E. Plonska-Brzezinska, A. Lapinski, A.Z. Wilczewska, A.T. Dubis, A. Villalta-Cerdas, K. Winkler, et al., The synthesis and characterization of carbon nano-onions produced by solution ozonolysis, Carbon 49 (2011) 5079–5089.
[44] E.G. Bushueva, P.S. Galkin, A.V. Okotrub, L.G. Bulusheva, N.N. Gavrilov, V.L. Kuznetsov, et al., Double layer supercapacitor properties of onion-like carbon materials, Phys. Status Solidi 245 (2008) 2296–2299.
[45] Y. Liu, D.Y. Kim, Enhancement of capacitance by electrochemical oxidation of nanodiamond derived carbon nano-onions, Electrochim. Acta 139 (2014) 82–87.
[46] S. Zhang, N. Sun, X. He, X. Lu, X. Zhang, Physical properties of ionic liquids: database and evaluation, J. Phys. Chem. Ref. Data 35 (2006) 1475–1517.
[47] A. Noda, K. Hayamizu, M. Watanabe, Pulsed-gradient spin - echo 1 H and 19 F NMR ionic diffusion coefficient, viscosity, and ionic conductivity of non-chloroaluminate room-temperature ionic liquids, J. Phys. Chem. B (2001) 4603–4610.
[48] T. Brousse, D. Belanger, J.W. Long, To be or not to be pseudocapacitive? J. Electrochem. Soc. 162 (2015) A5185–A5189.
[49] J. Romanos, M. Beckner, T. Rash, L. Firlej, B. Kuchta, P. Yu, et al., Nanospace engineering of KOH activated carbon, Nanotechnology 23 (2012) 1–7.
[50] K. Bogdanov, A. Fedorov, V. Osipov, T. Enoki, K. Takai, T. Hayashi, et al., Annealing-induced structural changes of carbon onions: high-resolution transmission electron microscopy and Raman studies, Carbon 73 (2014) 78–86.
[51] K. Pinkert, L. Giebeler, M. Herklotz, S. Oswald, J. Thomas, A. Meier, et al., Functionalised porous nanocomposites: a multidisciplinary approach to investigate designed structures for supercapacitor applications, J. Mater. Chem. A 1 (2013) 4904–4910.